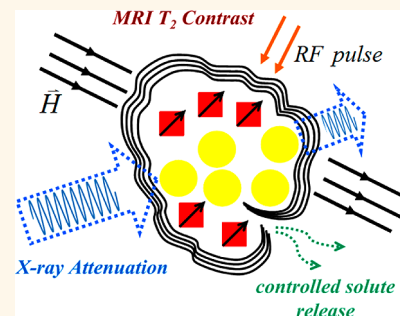


Encapsulation of Particle Ensembles in Graphene Nanosacks as a New Route to Multifunctional Materials

Yantao Chen,^{†,‡} Fei Guo,^{‡,§} Yang Qiu,[‡] Hiroe Hu,[‡] Indrek Kulaots,[‡] Edward Walsh,^{§,¶,||,¶,*} and Robert H. Hurt^{‡,||,¶,*}

[†]Department of Chemistry, [‡]School of Engineering, [§]Department of Neuroscience, [¶]Department of Diagnostic Imaging, ^{||}Institute for Molecular and Nanoscale Innovation, and [¶]Brown Institute for Brain Science, Brown University, Providence, Rhode Island 02912, United States. ^{*}These authors contributed equally.

ABSTRACT Hybrid nanoparticles with multiple functions are of great interest in biomedical diagnostics, therapies, and theranostics but typically require complex multistep chemical synthesis. Here we demonstrate a general physical method to create multifunctional hybrid materials through aerosol-phase graphene encapsulation of ensembles of simple unifunctional nanoparticles. We first develop a general theory of the aerosol encapsulation process based on colloidal interactions within drying microdroplets. We demonstrate that a wide range of cargo particle types can be encapsulated, and that high pH is a favorable operating regime that promotes colloidal stability and limits nanoparticle dissolution. The cargo-filled graphene nanosacks are then shown to be open structures that rapidly release soluble salt cargoes when reintroduced into water, but can be partially sealed by addition of a polymeric filler to achieve slow release profiles of interest in controlled release or theranostic applications. Finally, we demonstrate an example of multifunctional material by fabricating graphene/Au/Fe₃O₄ hybrids that are magnetically responsive and show excellent contrast enhancement as multimodal bioimaging probes in both magnetic resonance imaging and X-ray computed tomography in full-scale clinical instruments.



KEYWORDS: graphene oxide · encapsulation · imaging · multifunctional probe · controlled release · contrast agent

A major goal in nanochemistry is the synthesis of hybrid structures that exhibit multiple functions that cannot be achieved in single-phase, homogeneous nanomaterials. The functions may involve a combination of magnetic, photonic, radiological, electrical, fluorescent, and delivery behaviors,^{1–8} and the hybrid structures include core–shell,^{8–10} dumbbell,^{11,12} “patchy” particle assemblies,¹³ polymer-coated binary NPs,¹⁴ and basic geometries (spheres, cylinders, sheets) with adherent nanoclusters.¹⁵

One example application area is biomedical imaging, where nanoprobes are being developed for disease detection using magnetic resonance imaging (MRI), X-ray computed tomography (CT), positron emission tomography (PET), or fluorescence.^{12,14,16–18} Biomedical diagnostics often incorporate more than one imaging modality (e.g., MRI/fluorescence,^{1,19} MRI/radiological/fluorescence,²⁰ PET/CT⁵) or combine imaging diagnostics and therapies to produce hybrid materials for theranostics.^{8,10,21–23} MRI

and CT are now two of the most widely used noninvasive imaging techniques in clinical diagnostics, and several groups have reported dual-functional contrast agents.^{14,18}

Many multifunctional nanostructures combine different solid-phase chemistries in a single structure through a series of chemical synthesis steps, which become increasingly difficult as the complexity of the probe increases with corresponding decrease in yield. Recently, an aerosol-phase method has been demonstrated for encapsulating nanoparticles or macromolecules in graphene “nanosacks”.^{24–28} This process is simple, continuous, and scalable and would have the potential to become a general and flexible route for creation of multifunctional nanostructures if multiple cargo materials can be simultaneously and uniformly wrapped. To achieve this requires a better understanding of the aerosol encapsulation process, which determines the nature of the cargoes that can be successfully wrapped, the structure of the hybrid materials, and their solute

* Address correspondence to
robert_hurt@brown.edu,
edward_walsh@brown.edu.

Received for review December 3, 2012
and accepted April 6, 2013.

Published online April 06, 2013
10.1021/nn3055913

© 2013 American Chemical Society

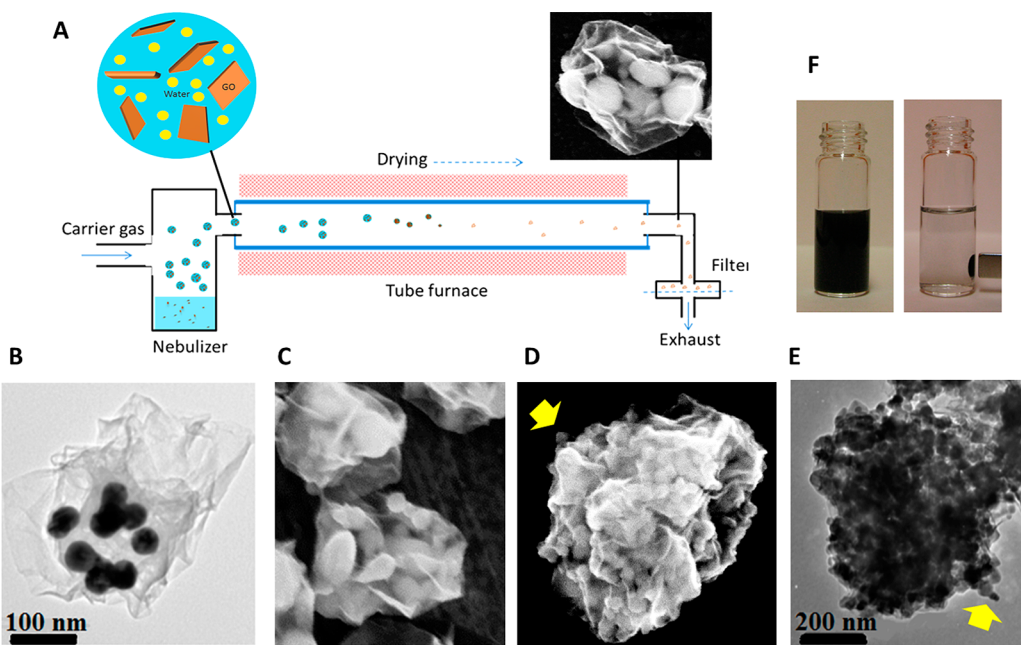


Figure 1. Aerosol-phase synthesis of cargo-filled graphene nanosacks and examples of binary materials with a single homogeneous cargo. (A) Continuous aerosol fabrication process leading to Ag-filled nanosacks.²⁴ (B–E) Electron micrographs of selected binary composite product structures (reduced GO with single cargo material). (B) Tannic-acid-capped AuNPs, (C) Si NPs, (D,E) Fe_3O_4 NPs, (F) Fe_3O_4 -filled nanosacks can be easily cleared from ethanol solution with a hand-held magnet demonstrating stable encapsulation and the absence of free rGO. The particles alone cannot be dispersed in ethanol, so the graphene oxide serves as both a dispersing and encapsulation agent in this case. Arrows on D and E show a minority of particles on or very near the outside surface of the Fe_3O_4 -filled nanosacks.

release characteristics relevant to delivery and theranostics.

In this article, we propose a new theory for the colloidal dynamics that govern aerosol-phase encapsulation by graphene oxide and extend the aerosol process to multiple cargo materials. We also show that the sacks are intrinsically open structures that rapidly release soluble cargoes into solvent environments but can be partially sealed to achieve slow release profiles. Finally, we demonstrate one example of a simple synthesis of a graphene/Au/ Fe_3O_4 ternary probe that is magnetically responsive and highly active as both an MRI and CT multimodal bioimaging contrast agent.

RESULTS AND DISCUSSION

A wide range of nanoparticles are of interest for application in multifunctional materials. We thus began by exploring the limits of the aerosol graphene encapsulation process for particle cargoes of differing type. Figure 1 shows the aerosol encapsulation process and example structures made from binary feed solutions, meaning those containing graphene oxide (GO) and one cargo particle type. Here an aqueous dispersion containing the cargo and graphene oxide is ultrasonically nebulized, and the microdroplet mist is carried by an inert gas flow through an electrically heated furnace. The dried nanosacks are collected on a polytetrafluoroethylene filter (Figure 1A), and in the most common experiment, the furnace temperature is set at 500–600 °C, converting the GO sack to

reduced graphene oxide (rGO). We observed successful encapsulation with many of these binary systems, but not all. Some systems formed gels or visible precipitates in the feed suspension that led to nonuniform products or significant numbers of isolated unwrapped nanoparticles (e.g., in the case of CuO NPs and Co NPs functionalized with L-cysteine ethyl ester). Other systems led to good encapsulation even though the nanoparticle cargoes did not form stable colloidal suspensions on their own in water (e.g., Fe_3O_4 , BaTiO_3). There are also subtle differences in structure among the successful cases, with some completely encapsulated with a high degree of sack–cargo segregation (Figure 1B), while others show particles that appear to be on the outer surface (arrows, Figure 1D,E). HRTEM on these systems reveals that some of the nanoparticles are in fact covered by very thin reduced graphene oxide films with a width of ~2 nm and are thus “inside” but in the near-surface region (Supporting Information, Figure S1). On the basis of these facts, we hypothesized that colloidal interactions involving the cargo particles and the graphene oxide sheets play an important role in successful aerosol encapsulation and the structure of the hybrid material products.

Our previous work²⁴ proposed a mechanism for sack–cargo formation, in which graphene oxide shows a thermodynamic preference to localize at the air–water interface and its large hydrodynamic size leads to slow diffusion away from the drying front. GO thus collects as a multilayer film at the droplet outer surface

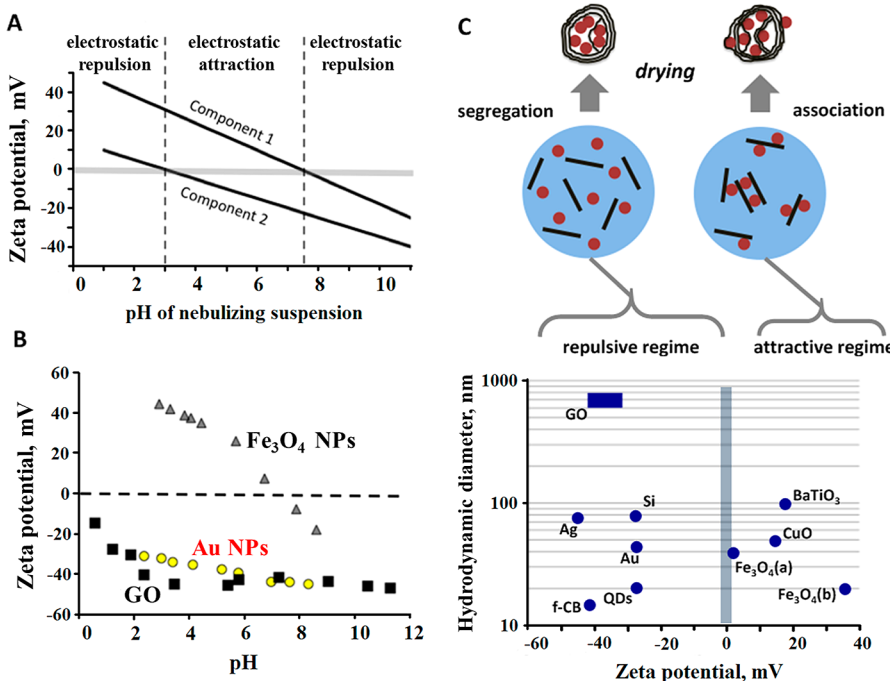


Figure 2. Proposed theory for colloidal sack–cargo assembly in binary systems: (A) pH-dependent zones of electrostatic attraction and repulsion (general behavior); (B) specific behaviors of graphene oxide and two example cargo materials. The acidic nature of GO gives it a negative colloidal surface charge over a wide pH range. Only one regime is seen for the GO/Au system and is repulsive. The GO/Fe₃O₄ system shows one attractive regime (pH < 7) and one repulsive regime (pH > 7). (C) Map of size and surface charge for sack–cargo systems studied here and proposed assembly mechanisms in the repulsive and attractive regimes. The hydrodynamic size of all cargoes is smaller than that of GO, allowing fast diffusion of the cargo away from the drying droplet front and thus diffusion segregation and sack–cargo separation in the colloidal repulsive regime where the particles act independently of the GO sheets.

and collapses by capillary forces in the late stages of drying. The NP cargoes in contrast diffuse away from the drying front to localize preferentially in the sack interior.²⁴ This theory was developed for citrate-capped Ag NPs, which show a large negative surface charge in common with GO, and the original theory was specific for such mutually repelling binary colloids. Some NPs of interest here in the larger sample set, however, have positive charge or are nearly isoelectric, and a more general theory is needed to understand the range of applicability of the aerosol technique and to explain the observations above.

Figure 2 shows the elements of a new, general theory of sack–cargo assembly that applies in different electrostatic regimes. The theory will be formulated for binary colloids but is easily extended to systems with three or more colloidal components. Figure 2A shows pH-dependent zeta-potentials for a generalized binary colloid, which give rise to three regimes: two electrostatically repulsive regimes at high and low pH, where colloidal stability and sack–cargo segregation are expected, and an attractive regime at intermediate pH, where complex association phenomena can occur between the colloidal particle components. To apply this to sack assembly, we measured zeta-potentials for all candidate cargo particles in deionized water, but the results were not directly relevant due to differences in pH between the single-component suspensions and

the binary suspensions containing GO. We therefore measured the pH of the GO/cargo nebulizing suspensions and measured zeta-potentials for GO and particles at the relevant mixture pH (Figure 2B). For GO itself, the net surface charge is negative between pH 2 and 12, and the potential/pH profile has a flat valley above pH 5, which suggests carboxylate groups as an important source of acidity and surface charge. Gold NPs were characterized as an example cargo and are also persistently negative due to their tannic acid capping. The GO/Au system shows only one of the three possible regimes, and its highly repulsive nature leads to good sack–cargo segregation. Iron oxide NPs show a zeta-potential with a strong pH dependence and an isoelectric point near 7.²⁹ The GO/Fe₃O₄ system thus shows two of the three possible regimes in Figure 2A. The pH of our GO/Fe₃O₄ suspensions varies with GO/Fe₃O₄ ratio and was measured as pH 3 for the case shown in Figure 1. At this pH, the Fe₃O₄ NPs have strongly positive surface charge and would associate with the negatively charged GO. The Derjaguin, Landau, Verwey, and Overbeek (DLVO) theory would predict no repulsive barrier to association (heteroaggregation) and indeed we see a single peak in zeta-potential measurement in GO/Fe₃O₄ suspensions. We also see a single zeta-potential peak for a variety of binary suspensions containing GO and NPs with positive surface charge at the mixture pH. We believe this association

explains the ability to disperse and encapsulate these Fe_3O_4 NPs, which are colloidally unstable in the absence of GO.³⁰ In general, the association of NPs with GO can aid in NP dispersion but may also lead to charge neutralization, GO–GO bridging, and aggregation. Small aggregates may be incorporated into the 5 μm droplets formed by ultrasound, but larger aggregates or gel networks cannot be uniformly nebulized into microdroplets, leading to poor encapsulation performance, as seen for CuO and Co under some conditions. In addition, some metal and metal oxide NPs are unstable to dissolution, including Ag,³¹ ZnO,³² and CuO.³³ We observed the zeta-potential of CuO/GO mixtures to be higher than either CuO or GO alone and to form gel phases, which we believe is due to CuO partial dissolution and Cu^{2+} binding to GO– COO^- groups that neutralize surface charge and destroy colloidal stability. We found that NaOH titration of GO/CuO NP suspension from pH 5.3 to 10 moves the system from the attractive regime to the repulsive regime and also suppresses oxide dissolution, allowing successful CuO encapsulation (Supporting Information, Figure S2). Titration to basic pH appears to be useful to avoid metal and metal oxide dissolution during encapsulation.

Figure 2C shows the range of NPs used in this study and a conceptual model of the assembly process in the attractive and repulsive regimes. The repulsive regime leads to separate GO and nanoparticle phases, whose differing diffusion rates lead to good sack–cargo separation during drying (Figure 1B). The attractive regime in contrast leads to GO–particle attachment, which reduces the degree of sack–cargo segregation and leads to the presence of some particles on the external surface or in the near-surface regime intercalated between graphene sheets, as seen in Figure 1D,E. This conceptual model explains why a wide variety of colloidal particles can be processed by the aerosol technique, including those that are colloidally unstable on their own. Another useful result of this model is that, when colloidal instability and/or poor encapsulation is observed, base titration to high pH is an effective technique to establish the repulsive regime where GO and the cargo particle both carry negative surface charges and form stable binary suspensions. A further benefit of base titration is the suppression of metal or metal oxide dissolution, which is typically proton-mediated.³¹

Nanosack Sealing and Controlled Release. A second fundamental issue to resolve in nanosack technology relates to nanosack sealing and internal solute release. If graphene nanosacks are hermetically sealed, this would be useful for biological application of acutely toxic cargoes, which can be isolated from tissue by the graphene sack acting as a barrier. If, however, the sacks are open to small molecule transport, then applications as catalyst supports, electrode materials, drug delivery vehicles, and theranostics are possible. Several

independent assays were devised to characterize nano-sack sealing and solute exchange. First we studied nitrogen vapor adsorption on nanosacks filled with Fe_3O_4 NPs as a probe for the accessibility of internal pores and surfaces. Figure 3B shows the pore size distribution of Fe_3O_4 -filled graphene nanosacks obtained from nitrogen vapor adsorption data analyzed by non-local density functional theory (DFT) using a carbon slit pore model.³⁴ There is a characteristic mesopore size of about 4 nm, which is similar to that seen in the empty sacks and possibly attributed to the inner space in loop-shaped ridges seen by SEM and TEM.²⁴ The Fe_3O_4 -filled graphene nanosacks have a total accessible surface area of 78 m^2/g and about 0.5 cm^3/g of total pore volume (Figure 3A). Using a true density of 1.8 g/cm^3 for reduced graphene oxide, the porosity, $V_{\text{pores}}/V_{\text{total}}$, is estimated to be 0.66, which suggests that the internal spaces are open to the N_2 adsorbate. The surface area and pore volume of the Fe_3O_4 -filled nanosacks lie between those of the empty sacks and the Fe_3O_4 nanoparticles alone as a bulk powder and are roughly consistent with a simple additive relationship for the relevant Fe_3O_4 /graphene mass ratio, which is 5.7:1.

This significant pore volume suggests the sacks are open, though these data alone do not indicate whether the pores connect the particle exterior to the internal cargo. Evidence for this connection comes from acid dissolution studies (Figure S3). Immersing the Fe_3O_4 -filled sacks in HCl is seen to etch away the internal particles, leaving the sack intact (Figure S3). Further, cesium chloride was used as model solute to study release from the sack interior. We found that exposing CsCl-filled graphene nanosacks to humid room air prior to SEM analysis led to water uptake and the release of salts clearly seen in Figure 3C. The highly hygroscopic nature of these sacks comes from the fact that high surface area nanocrystals of the highly soluble CsCl are exposed to ambient water vapor. In Figure 3D, we use a chloride-specific electrode to measure release kinetics. Release from the as-produced nanosacks is too fast to measure with this technique (<10 s). The rapid release in the as-produced sacks is consistent with pore transport over these length scales. With the relevant particle length scale of 100 nm, a porosity values of 0.66 and a Cl^- aqueous diffusion coefficient of $2 \times 10^{-5} \text{ cm}^2/\text{s}$,³⁵ characteristic diffusion times, L^2/D , are predicted to be on order of 7 μs if the pores connect the cargo space with the exterior. Each of these tests indicates that the sacks are open and capable of quickly releasing small molecule cargoes.

Delivery or theranostic applications will require controlled release behavior rather than the rapid release observed for as-produced sacks. As a proof-of-principle, we added carboxymethyl cellulose (CMC) to see if an additional filler material could provide a diffusion barrier to achieve slow release of the CsCl salt probe. Addition of CMC to the nebulizing suspension led to rGO/CsCl/CMC nanosacks (Figure S4), and the 500 °C drying

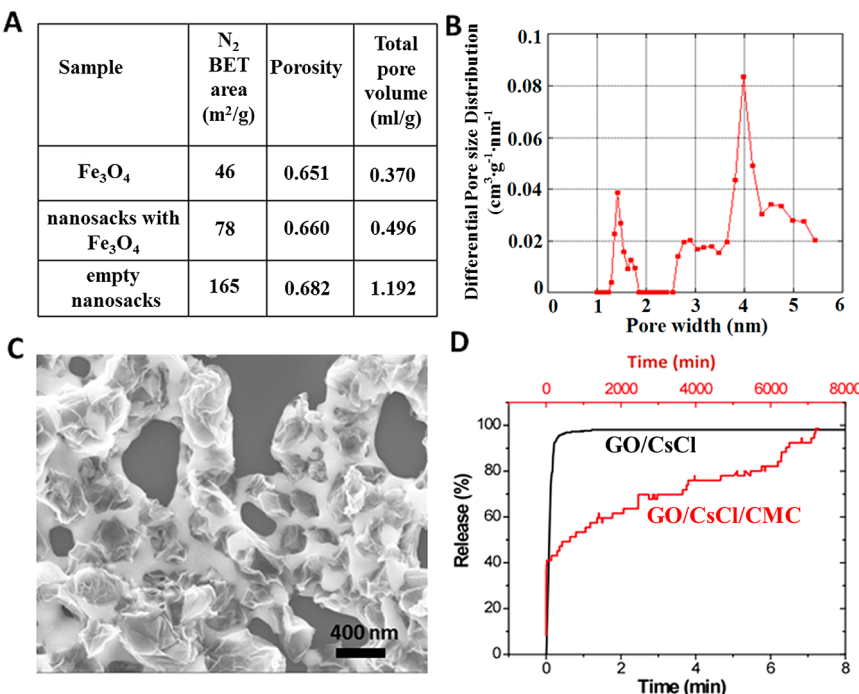


Figure 3. Information on graphene nanosack sealing and solute release as relevant to delivery functions. (A) Brunauer–Emmett–Teller (BET) surface area, porosity, and pore volume of Fe₃O₄, empty nanosacks, and Fe₃O₄-filled nanosacks. **(B)** Pore size distribution of Fe₃O₄-filled nanosacks obtained from nitrogen vapor adsorption isotherms by applying nonlocal density functional theory (DFT) with a carbon slit pore model. **(C)** SEM of CsCl-filled graphene nanosacks after brief exposure to humid air. Salt-filled sacks (GO/CsCl mass ratio 1:4) are highly hygroscopic and take up atmospheric moisture and release CsCl to form visible salt films surrounding the sacks. **(D)** Chloride release rate in DI water for CsCl-filled nanosacks with and without carboxymethylcellulose (CMC) as a sealing additive. CMC addition to the aerosol process reduces the dissolution rate of soluble CsCl.

temperature decomposes CMC to volatile matter and carbon filler. Figure 3D shows that a portion of the salt release now occurs over much longer time scales, on the order of days. The ability to add water-soluble solutes and fillers to graphene nanosacks opens up the possibility for controlled release applications either alone or in combination with diagnostic functions.

Example Multimodal Probes. The theory for binary colloids presented in Figure 2 is easily extended to systems with $N_{\text{components}} > 2$, which is the regime of interest for multifunctional materials. We chose to demonstrate the multicomponent capability by fabricating dual-purpose magnetically responsive contrast agents for both MRI and X-ray CT. MRI and CT are two of the most widely used techniques in clinical diagnostics and can be applied alone or in combination.³⁶ Due to its good availability and relatively low costs, CT is often the preferred technique for pretreatment evaluation of cancer and offers high patient throughput and high-resolution imaging.³⁷ MRI is a flexible technique that identifies pathology based upon their difference on T_1 , T_2 (or T_2^*) relaxation time and proton density between diseased and normal tissue. Figure 4A–C shows three different multicomponent graphene sacks of interest in dual CT/MRI imaging, based on rGO/Au/Fe₃O₄ or rGO/BaTiO₃/Fe₃O₄ chemistries. Each of the materials was fabricated with a component mass ratio of 1:2:2. The multicomponent nature of these hybrid is most easily

seen in Figure 4B, in which the lower electron density and small size of the Fe₃O₄ NPs distinguish them from Au, and in Figure 4C, where the large size of BaTiO₃ NPs distinguishes them from the Fe₃O₄ NPs. High-resolution TEM, Raman, and XRD show that the graphene sack is a multilayer structure that conforms to particles in the peripheral region and bridges open spaces between neighboring particles (Figure 4D and Figure S5).

The magnetic properties of one set of rGO/Au/Fe₃O₄ nanosacks were characterized by vibrating sample magnetometry on 15 mg dry powder samples (Supporting Information, Figure S6). We observe a small degree of hysteresis, which is consistent with the 50 nm size of the iron oxide nanoparticles in these sacks, and the remanence and coercivity were determined to be 1.040 emu/g and 0.01416 T, respectively. The saturation magnetization was not reached at the maximum applied field of 0.8T, but the maximum developed magnetization noted was 4.52 emu/g at 0.8T. This developed magnetization is substantially larger than that produced by ferritin cage-based iron and manganese contrast agents by a factor of 11.3 and 2.26, respectively.^{38,39} Use of single domain superparamagnetic particles as the cargo (8–10 nm) may result in a larger developed magnetization, smaller hysteresis, and even greater T_2 contrast effect.

Figure 5 shows the MRI and CT contrast performances of the G/Au, G/Fe₃O₄, and three-way rGO/Au/Fe₃O₄ hybrids. The filled graphene nanosacks were suspended

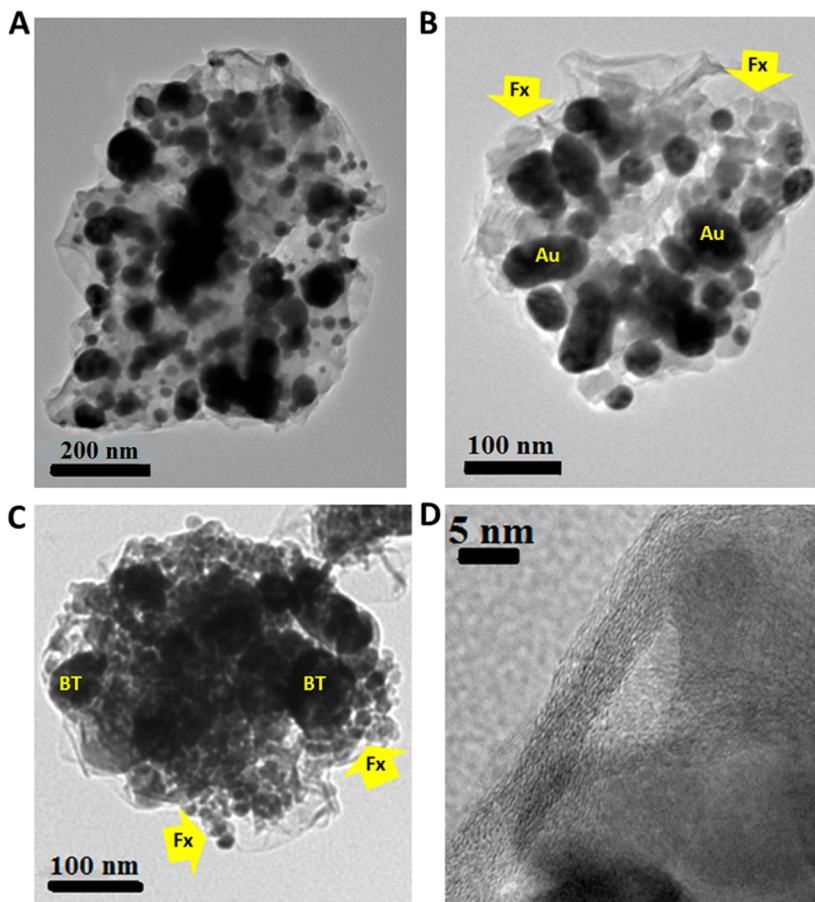


Figure 4. Example multifunctional probes as dual CT/MRI contrast agents. (A) rGO/Au/Fe₃O₄ hybrid used in the magneto-metry and MRI/CT characterization in Figure 5. (B) Second rGO/Au/Fe₃O₄ hybrid with 20 nm Fe₃O₄ NPs ("Fx") whose small size and low electron density make them visually distinct from the nominal 40 nm Au. (C) rGO/BaTiO₃/Fe₃O₄ hybrid for GI tract imaging. (D) High-resolution image of a multilayer graphene sheet bridging two cargo particles at the outer edge of an rGO/Fe₃O₄ structure.

in carboxymethylcellulose (CMC) gel in cylindrical 5 mL tubes at a series of increasing concentrations and placed horizontally in the MRI and CT test zones for cross-sectional imaging relative to gel-only controls. Figure 5A,B shows the MRI behavior of the rGO/Fe₃O₄ nanosacks, in the form of *T*₂-weighted images with an echo time of 30 ms along with a *T*₂ map computed using the monoexponential fit to the 24-echo data. The Fe₃O₄-filled nanosacks show a strong *T*₂ contrast effect at parts per million doses. From a gel control mean *T*₂ of 535 ms, *T*₂ monotonically decreased with increasing concentration, reaching a value of 19.1 ms at the concentration of 50 μ g/mL. The relaxation rate ($R_2 = 1/T_2$) is linear with dose, as expected (Supporting Information, Figure S7). Computing relaxivity as the slope of this line gives $r_2 = 1012 \text{ s}^{-1} (\text{mg/mL})^{-1}$. There was also a weak *T*₁ effect with an estimated relaxivity $r_1 = 4.95 \text{ s}^{-1} (\text{mg/mL})^{-1}$. This behavior is expected, as iron-oxide-based contrast agents are used primarily to reduce *T*₂ and *T*₂^{*}, although some *T*₁ effect has been described previously.⁴⁰ The three-way G/Au/Fe₃O₄ hybrid shows similar behavior (Figure 5C) but with reduced relaxivity ($r_2 = 114.0 \text{ s}^{-1} (\text{mg/mL})^{-1}$) relative to the pure Fe₃O₄ cargo. The hybrid's

effect on *T*₁ was practically negligible with a reduction in *T*₁ of 9.5% below the gel control at a concentration of 500 μ g/mL.

Figure 5D,E shows the X-ray CT contrast performance for the G/Au hybrids, Au particle control, and gel-only control. The maximum attenuation was noted at 80 kVp with a mean CT number increase of 57.8 for the 2000 μ g/mL Au/nanosack sample. The same concentration for free gold (no nanosacks) produced at mean CT number change of 102, which is consistent with the increased mass fraction of Au in this material. The expected monotonic decrease in attenuation with increasing kVp was interrupted at 120 kVp. This is probably a consequence of the K-edge absorption of gold at 80.725 keV. With an X-ray tube voltage bias of 120 kVp, there was a sufficiently large number of photons in the region of 80 keV to allow observation of K-edge attenuation. As expected, a reduction in the quantity of gold in the nanosacks reduced the observed attenuation, with a mean CT number change of 25.6 at a concentration of 2000 μ g/mL at 80 kVp (Figure 5E). Again, there is an increase in attenuation going from 100 to 120 kVp,

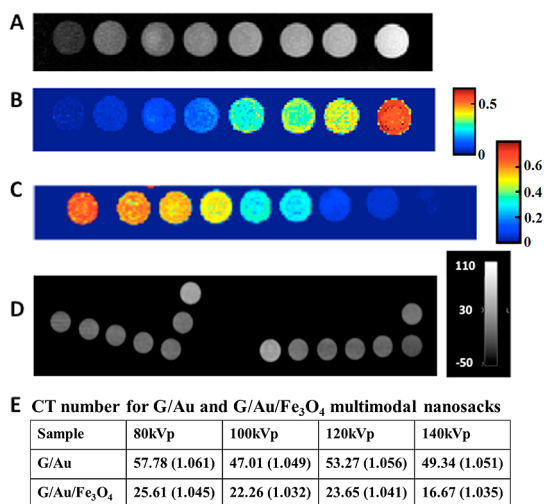


Figure 5. Clinical MRI and X-ray CT results showing the contrast performance of rGO/Fe₃O₄, rGO/Au, and rGO/Au/Fe₃O₄ multifunctional probes. (A) T₂-weighted image (TE = 30 ms) of rGO/Fe₃O₄ nanosacks in CMC gel. Control (gel alone) is on the right, with nanosack concentration increasing right to left: 0.5, 1, 2, 5, 10, 20, 50, μ g/mL. (B) T₂ map computed from the 24 echo image series. Color bar is T₂ in seconds. (C) MRI T₂ map of the G/Au/Fe₃O₄ hybrid. Sack concentrations increase from left to right as 0.05, 0.1, 0.5, 1, 5, 10, 50, 100, and 500 μ g/mL. (D) X-ray CT image (80 kVp) of the G/Au nanosacks (right-hand L-shaped sequence) and free Au controls (left-hand L-shaped sequence). For the G/Au nanosacks, the sack concentrations in μ g/mL from left to right are 2000, 400, 200, 40, 20, gel control, H₂O control. For the free Au, the particle concentrations are (left to right) 400, 200, 40, 20, gel control with the 2000 μ g/mL sample at the top, and a 200 μ g/mL sample of empty sacks immediately beneath it. (E) Table of CT results shown as change in CT number with the attenuation (relative to control gel sample) shown in parentheses.

again indicating the possibility of the K-edge attenuation effect.

The imaging results demonstrate the feasibility of cargo-filled graphene nanosacks as contrast agents applicable to MRI and X-ray CT and the potential for development of versions suitable for use with both modalities. Note that the degree of T₂ effect is believed to be influenced by water penetration into and out of the nanosack, as is the case for modified ferritin complexes.^{38,39} The further development of this application will require optimization of cargoes (single domain magnetic particles), nanosack size (through concentration and droplet size optimization), and functionalization and targeting of the nanosack exterior through well-known coupling chemistries for graphene and related carbon materials.^{41–44} Further applications may be in spatial frequency heterodyne imaging,⁴⁵

which offers promise for use of X-ray scattering in the imaging of object edges with abrupt changes in phase or absorption with low concentrations of the absorbing agent such as gold.

CONCLUSIONS

These results show that graphene encapsulation in the aerosol phase is a useful new technique for fabrication of multifunctional materials. Ensembles of simple unifunctional nanoparticles can be wrapped by graphene in a nonchemically specific manner to produce multifunctional structures without the need for complex multistep chemical synthesis. A wide variety of nanoparticle cargoes can be encapsulated this way, including some that are colloidally unstable on their own but become stable through electrostatic association with GO sheets. In some cases, particle/sheet association becomes extensive and large heteroaggregates form that disrupt uniform aerosol formation and encapsulation. In these cases, high pH is shown to be the favorable operating regime where GO and most nanoparticle cargoes have common negative surface charge and thus disperse uniformly and independently. High pH also enhances the stability of some metal and metal oxide NPs to dissolution or oxidative dissolution. This study also shows that graphene sacks in as-produced form are open to small solute exchange with their environment but can be partially sealed by addition of polymer filler to the nebulizing suspension. The partial sealing suggests potential for controlled release applications and their combination with multimodal imaging as demonstrated here toward the goal of graphene nanosack-based theranostics.

Finally, this study demonstrates the multifunctional materials concept by fabricating rGO/Au/Fe₃O₄ and rGO/BaTiO₃/Fe₃O₄ ternary particles as MRI/CT multimodal imaging probes. The graphene/Au/Fe₃O₄ probe shows both MRI and CT contrast in CMC gel suspensions at low concentrations ranging from 0.05 to 2000 μ g/mL based on tests using clinical-scale scanners. While this first experiment demonstrated both MRI and CT contrast, further work is needed to develop multimodal probes for specific applications. We envision the optimization of cargoes, by using smaller Fe₃O₄ nanoparticles for increased developed magnetization,^{46,47} and the use of smaller nanosacks with higher number densities for improved vascular penetration to tumors through the enhanced permeability and retention effect.

MATERIALS AND METHODS

Materials. Graphene oxide was prepared, purified, and characterized using a modified Hummer's method as described previously.^{48,49} Fe₃O₄ and CuO NPs were purchased from Sigma Aldrich with a particle size of <50 nm; 20 nm Fe₃O₄ and 50 nm

BaTiO₃ NPs were purchased from U.S. Research Nanomaterials Inc. Au NPs were synthesized with a modified method reported by Hayat *et al.*,⁵⁰ by the reduction of 50 mL of HAuCl₄ in the presence of citrate and tannic acids.

Aerosol Encapsulation Process. Colloidal suspensions of GO (0.5 mg/mL) and one or more cargo nanoparticles were sonicated

together for dispersion and then ultrasonically nebulized into aerosol microdroplets (nebulizing feed rate: 10 mL/h) suspended in nitrogen gas (0.7 L/min) and passed directly into a horizontal benchtop electric tube furnace operated at a peak temperature of 600 °C as explained in Chen *et al.*²⁴ The products, which are cargo-filled graphene nanosacks, were collected on a heated (~90 °C) Teflon filter (PTU024750, Sterlitech Co.) or onto a small silicon wafer chip (5 × 5 mm, Ted Pella, Inc.) or copper grid (Ted Pella, Inc.) placed on top for SEM or TEM analysis. The experiments with salt cargoes (graphene/CsCl nanosacks) used a peak temperature of 500 °C. The controlled release experiments used nebulizing feed suspensions containing GO, CsCl, and the water-soluble polymer sodium carboxymethylcellulose (Sigma Aldrich) at a mass ratio CMC/GO/CsCl of 0.5:1:4. The primary drying temperature was reduced to 80–100 °C and followed by post-carbonization of CMC at 500 °C by slow heating in a batch tube furnace for 30 min.

Characterization. SEM (LEO 1530 VP at 15 kV), TEM (Philips CM 20 at 200 kV), and HRTEM (JEOL JEM-2010 at 200 kV) were carried out at the Brown IMNI Electron Microscopy Facility. Zeta-potential and particle size distributions were measured in DI water using a Malvern Nano-ZS dynamic light scattering instrument. Before measuring the zeta-potential, the pH value of the suspension was measured by using an Orion 5-Star Plus pH/ORP/ISE/conductivity/DO meter (Thermo Scientific Inc.). Prior to zeta-potential measurement, the pH values of nanoparticle suspensions were adjusted with 0.1 M NaOH or 0.1 M HCl to match the pH in the binary suspensions used in the nebulizer feed. A Quantachrome Autosorb-1 instrument was used to measure N₂ vapor isotherms at 77 K, from which Brunauer–Emmett–Teller (BET) surface areas and pore size distributions applying nonlocal density functional theory (DFT) with a carbon slit pore model³⁴ were calculated.

Experiments on Solute Exchange and Controlled Release. The ability of small solutes to enter sacks was tested by immersing the Fe₃O₄-filled sacks (Figure 1D,E) into aqueous 0.1 M HCl followed by DI water washing to remove iron chloride salts. The sacks were visualized before and after acid leaching and EDS used to detect residual iron cargo. The release profile of soluble CsCl salt cargo from the sack interiors into DI water was measured using a Vernier ionic conductivity probe, which was precalibrated with standard CsCl aqueous solutions. In the experiments that included CMC, a chloride-ion-selective electrode (Vernier) was also used to eliminate the possibility that uncarbonized CMC as a charged solute would contribute to the observed conductivity.

MRI/CT/Magnetometry. A dry sample of the hybrid Au/Fe₃O₄-loaded graphene nanosacks was assessed for developed (saturation) magnetization and hysteresis (retentivity and coercivity) using a vibrating sample magnetometer (Lakeshore VSM model 7300). A 15 mg sample was placed in a 5 mm plastic capsule with a PTFE plug to constrain the material. The applied magnetic field strength was swept from −0.8 to 0.8 T while 441 measurements were taken. Three versions of loaded nanosacks were assessed for imaging properties: iron oxide nanoparticles (Fe₃O₄) as an MRI agent, gold nanoparticles as an X-ray CT agent, and a hybrid Au/Fe₃O₄ version for multimodal X-ray and MRI application. The hybrid sample was the same one used for the magnetometry assessment. Iron oxide is used in clinically approved MRI T₂ agents and produced a strong susceptibility effect. Gold is being investigated for use in nanoparticle contrast and therapy agents owing to its strong X-ray attenuation and scattering properties. The mass attenuation coefficient of gold at 100 keV is 5.16 cm²/g, which is 93% that of lead for the same photon energy.^{51,52}

For MRI, nanosacks filled with Fe₃O₄ or Au/Fe₃O₄ nanoparticles were suspended in CMC gel (1%) at concentrations of 0.5, 1, 2, 5, 10, 20, and 50 μg/mL for Fe₃O₄ and 0.05, 0.1, 0.5, 1, 5, 10, 50, 100, 500, and 2000 μg/mL for the hybrid. These preparations were placed in 5 mL vials along with control preparations of the same concentrations but not containing graphene nanosacks. In addition, control samples were included in the form of distilled water and gel with no added material. MRI data were acquired at the Brown University Magnetic Resonance Facility using a 3 T Siemens Tim Trio scanner. Samples were placed in a 32 channel receive resonator, and the volume body resonator was used for transmit. Cross section tomographic images were obtained using a spin echo acquisition for mapping T₂.

T₁-weighted images were obtained using an inversion recovery contrast preparation prior to the spin echo readout. An inversion recovery series was used for mapping T₁. Slice thickness was 3 mm, and first-order shimming was performed to optimize static magnetic field homogeneity over the samples. In-plane resolution was 0.7 mm using a 256 × 256 reconstruction matrix. Repetition time for the spin echo acquisition was 2000 ms and 4000 ms for the inversion recovery series. Echo times for the spin echo acquisition ranged from 10 to 240 ms in 10 ms steps (24 echoes). For the inversion recovery series, inversion delay times were 100, 200, 300, 400, 600, 1000, and 2000 ms. Relaxation time constant maps (T₁, T₂) were computed on a pixel basis using three-parameter least-squares fits to the signal equations:

$$\begin{aligned} S(\text{TE}) &= S_0 e^{-\text{TE}/T_2} \\ S(\text{TI}) &= S_0 (1 - 2e^{-\text{TI}/T_1} + e^{-\text{TR}/T_1}) \end{aligned} \quad (1)$$

where S₀ is the equilibrium (maximum possible) magnetization signal, TE is the echo time (for the spin and gradient echo acquisitions), TR is the repetition time, and TI is the inversion time. Relaxation rate maps were taken as the reciprocals of the relaxation time constant maps (e.g., R₂ = 1/T₂) for computation of relaxivity (change in relaxation rate per unit change in concentration of agent).

For X-ray CT studies, the same G/Au and G/Au/Fe₃O₄ samples were used as for MRI. For the G/Au sample, concentrations of 20, 40, 200, 400, and 2000 μg/mL were used. A General Electric LightSpeed VCT scanner (Department of Diagnostic Imaging, Rhode Island Hospital) was used for acquisition of tomographic cross section images, providing the same view as produced by the MRI scans. Slice thickness was 3 mm with a reconstruction matrix of 512 × 512 and an in-plane resolution of 0.5 mm. The X-ray tube current was 200 mAs. Images were acquired for X-ray tube voltages of 80, 100, 120, and 140 kVp. Contrast was determined as the difference in CT number (Hounsfield units) between the control gel sample and the samples containing contrast material. CT numbers were taken as the means of circular regions of interest from the center 80% of the cross sections. Hounsfield units are related to X-ray attenuation coefficient by

$$\text{CT}(x, y) = 1000 \left(\frac{\mu(x, y) - \mu_{\text{H}_2\text{O}}}{\mu_{\text{H}_2\text{O}}} \right) \quad (2)$$

where μ is the attenuation coefficient and $\mu_{\text{H}_2\text{O}}$ is the attenuation coefficient for water. The Hounsfield unit scale is normalized such that the attenuation of air corresponds to a CT number of −1000; the CT number of water is 0, with dense bone having a CT number of approximately 3000. In X-ray CT images, the pixel intensities are the CT numbers corresponding to the pixel locations.

Conflict of Interest: The authors declare no competing financial interest.

Acknowledgment. The authors acknowledge financial support from the Rhode Island Science and Technology Advisory Council (A. Bose, PI), the Brown–Yale Center for Chemical Innovation (NSF Award CHE-1240020), and NSF Grant CBET-1132446. The authors are also grateful to Professors Gang Xiao and Vesna Mitrovic at Brown University for assistance with the magnetometry, Jeomsoon Kim at Rhode Island Hospital Department of Diagnostic Imaging for help with CT, and Tony McCormick at Brown for assistance with electron microscopy.

Supporting Information Available: Additional electron microscopy characterization of Fe₃O₄- and CuO-filled graphene nanosacks and magnetometry data and analysis for the Fe₃O₄-filled sacks. This material is available free of charge via the Internet at <http://pubs.acs.org>.

REFERENCES AND NOTES

1. Kircher, M. F.; Mahmood, U.; King, R. S.; Weissleder, R.; Josephson, L. A Multimodal Nanoparticle for Preoperative Magnetic Resonance Imaging and Intraoperative Optical Brain Tumor Delineation. *Cancer Res.* **2003**, *63*, 8122–8125.

2. Lee, J.; Jun, Y.; Yeon, S.; Shin, J.; Cheon, J. Dual-Mode Nanoparticle Probes for High-Performance Magnetic Resonance and Fluorescence Imaging of Neuroblastoma. *Angew. Chem., Int. Ed.* **2006**, *45*, 8160–8162.
3. Anker, J. N.; Kopeelman, R. Magnetically Modulated Optical Nanoprobes. *Appl. Phys. Lett.* **2003**, *82*, 1102–1104.
4. Sokolov, K.; Follen, M.; Aaron, J.; Pavlova, I.; Malpica, A.; Lotan, R.; Richards-Kortum, R. Real-Time Vital Optical Imaging of Precancer Using Anti-epidermal Growth Factor Receptor Antibodies Conjugated to Gold Nanoparticles. *Cancer Res.* **2003**, *63*, 1999–2004.
5. Nahrendorf, M.; Zhang, H.; Hembrador, S.; Panizzi, P.; Sosnovik, D. E.; Aikawa, E.; Libby, P.; Swirski, F. K.; Weissleder, R. Nanoparticle PET-CT Imaging of Macrophages in Inflammatory Atherosclerosis. *Circulation* **2008**, *117*, 379–387.
6. Schluep, T.; Hwang, J.; Hildebrandt, I. J.; Czernin, J.; Choi, C. H.; Alabi, C. A.; Mack, B. C.; Davis, M. E. Pharmacokinetics and Tumor Dynamics of the Nanoparticle IT-101 from PET Imaging and Tumor Histological Measurements. *Proc. Natl. Acad. Sci. U.S.A.* **2009**, *106*, 11394–11399.
7. Cho, K. J.; Wang, X.; Nie, S. M.; Chen, Z.; Shin, D. M. Therapeutic Nanoparticles for Drug Delivery in Cancer. *Clin. Cancer Res.* **2008**, *14*, 1310–1316.
8. Cho, N.; Cheong, T.; Min, J. H.; Wu, J. H.; Lee, S. J.; Kim, D.; Yang, J.; Kim, S.; Kim, Y. K.; Seong, S. A Multifunctional Core–Shell Nanoparticle for Dendritic Cell-Based Cancer Immunotherapy. *Nat. Nanotech.* **2011**, *6*, 675–682.
9. Hirsch, L. R.; Stafford, R. J.; Banks, J. A.; Sershen, S. R.; Rivera, B.; Price, R. E.; Hazle, J. D.; Halas, N. J.; West, J. L. Nanoshell-Mediated Near-Infrared Thermal Therapy of Tumors under Magnetic Resonance Guidance. *Proc. Natl. Acad. Sci. U.S.A.* **2003**, *100*, 13549–13554.
10. Ji, X.; Shao, R.; Elliott, A. M.; Stafford, R. J.; Esparza-Coss, E.; Banks, J. A.; Liang, G.; Luo, Z.; Park, K.; Markert, J. T.; et al. Bifunctional Gold Nanoshells with a Superparamagnetic Iron Oxide–Silica Core Suitable for Both MR Imaging and Photothermal Therapy. *J. Phys. Chem. C* **2007**, *111*, 6245–6251.
11. Li, Y.; Zhang, Q.; Nurmiikko, A. V.; Sun, S. Enhanced Magneto-optical Response in Dumbbell-like Ag-CoFe₂O₄ Nanoparticle Pairs. *Nano Lett.* **2005**, *5*, 1689–1692.
12. Xu, C.; Xie, J.; Ho, D.; Wang, C.; Kohler, N.; Walsh, E. G.; Morgan, J. R.; Chin, Y. E.; Sun, S. Au-Fe₃O₄ Dumbbell Nanoparticles as Dual-Functional Probes. *Angew. Chem., Int. Ed.* **2007**, *47*, 173–176.
13. Hermans, T. M.; Broeren, M. A.; Gomopoulos, N.; van der Schoot, P.; van Genderen, M. H.; Sommerdijk, N. A.; Fytas, G.; Meijer, E. W. Self-Assembly of Soft Nanoparticles with Tunable Patchiness. *Nat. Nanotech.* **2009**, *4*, 721–726.
14. Kim, D.; Yu, M. K.; Lee, T. S.; Park, J. J.; Jeong, Y. Y.; Jon, S. Amphiphilic Polymer-Coated Hybrid Nanoparticles as CT/MRI Dual Contrast Agents. *Nanotechnology* **2011**, *22*, 155101.
15. Tran, P. A.; Sarin, L.; Hurt, R. H.; Webster, T. J. Titanium Surfaces with Adherent Selenium Nanoclusters as a Novel Anticancer Orthopedic Material. *J. Biomed. Mater. Res., Part A* **2010**, *93A*, 1417–1428.
16. Weissleder, R.; Pittet, M. J. Review Article Imaging in the Era of Molecular Oncology. *Nature* **2008**, *452*, 580–589.
17. Hahn, M. A.; Singh, A. K.; Sharma, P.; Brown, S. C.; Moudgil, B. M. Nanoparticles as Contrast Agents for *In-Vivo* Bioimaging: Current Status and Future Perspectives. *Anal. Bioanal. Chem.* **2011**, *399*, 3–27.
18. van Schooneveld, M. M.; Cormode, D. P.; Koole, R.; van Wijngaarden, J. T.; Calcagno, C.; Skajaa, T.; Hilhorst, J.; 't Hart, D. C.; Fayad, Z. A.; Mulder, W. J.; et al. A Fluorescent, Paramagnetic and PEGylated Gold/Silica Nanoparticle for MRI, CT and Fluorescence Imaging. *Contrast Media Mol. Imaging* **2010**, *5*, 231–236.
19. Veiseh, O.; Sun, C.; Gunn, J.; Kohler, N.; Gabikian, P.; Lee, D.; Bhattacharai, N.; Ellenbogen, R.; Sze, R.; Hallahan, A.; et al. Optical and MRI Multifunctional Nanoprobe for Targeting Gliomas. *Nano Lett.* **2005**, *5*, 1003–1008.
20. Patel, V.; Papineni, R. V.; Gupta, S.; Stoyanova, R.; Ahmed, M. M. A Realistic Utilization of Nanotechnology in Molecular Imaging and Targeted Radiotherapy of Solid Tumors. *Radiat. Res.* **2012**, *177*, 483–495.
21. Gobin, A. M.; Lee, M. H.; Halas, N. J.; James, W. D.; Drezek, R. A.; West, J. L. Near-Infrared Resonant Nanoshells for Combined Optical Imaging and Photothermal Cancer Therapy. *Nano Lett.* **2007**, *7*, 1929–1934.
22. Bagalkot, V.; Zhang, L.; Levy-Nissenbaum, E.; Jon, S.; Kantoff, P. W.; Langer, R.; Farokhzad, O. C. Quantum Dot–Aptamer Conjugates for Synchronous Cancer Imaging, Therapy, and Sensing of Drug Delivery Based on Bi-Fluorescence Resonance Energy Transfer. *Nano Lett.* **2007**, *7*, 3065–3070.
23. Kirui, D. K.; Rey, D. A.; Batt, C. A. Gold Hybrid Nanoparticles for Targeted Phototherapy and Cancer Imaging. *Nanotechnology* **2010**, *21*, 105.
24. Chen, Y.; Guo, F.; Jachak, A.; Kim, S. P.; Datta, D.; Liu, J.; Kulaots, I.; Vaslet, C.; Jang, H. D.; Huang, J.; et al. Aerosol Synthesis of Cargo-Filled Graphene Nanosacks. *Nano Lett.* **2012**, *12*, 1996–2002.
25. Luo, J.; Zhao, X.; Wu, J.; Jang, H. D.; Kung, H. H.; Huang, J. Crumpled Graphene-Encapsulated Si Nanoparticles for Lithium Ion Battery Anodes. *J. Phys. Chem. Lett.* **2012**, *3*, 1824–1829.
26. Sohn, K.; Na, Y. J.; Chang, H.; Roh, K.; Jang, H. D.; Huang, J. Oil Absorbing Graphene Capsules by Capillary Molding. *Chem. Commun.* **2012**, *48*, 5968–5970.
27. Mao, S.; Wen, Z.; Kim, H.; Lu, G.; Hurley, P.; Chen, J. A General Approach to One-Pot Fabrication of Crumpled Graphene-Based Nanohybrids for Energy Applications. *ACS Nano* **2012**, *6*, 7505–7513.
28. Jang, H. D.; Kim, S. K.; Chang, H.; Roh, K. M.; Choi, J. W.; Huang, J. A Glucose Biosensor Based on TiO₂-Graphene Composite. *Biosens. Bioelectron.* **2012**, *38*, 184–188.
29. Dao, T. J.; Pourroy, G.; Greeneche, J. M.; Bertin, A.; Felder-Flesch, D.; Begin-Colin, S. Water Soluble Dendronized Iron Oxide Nanoparticles. *Dalton Trans.* **2009**, 4442–4449.
30. Kim, J.; Cote, L. J.; Kim, F.; Yuan, W.; Shull, K. R.; Huang, J. Graphene Oxide Sheets at Interfaces. *J. Am. Chem. Soc.* **2010**, *132*, 8180–8186.
31. Liu, J.; Hurt, R. H. Ion Release Kinetics and Particle Persistence in Aqueous Nano-Silver Colloids. *Environ. Sci. Technol.* **2010**, *44*, 2169–2175.
32. Miao, A. J.; Zhang, X. Y.; Luo, Z.; Chen, C. S.; Chin, W. C.; Santschi, P. H.; Quigg, A. Zinc Oxide-Engineered Nanoparticles: Dissolution and Toxicity to Marine Phytoplankton. *Environ. Toxicol. Chem.* **2010**, *29*, 2814–2822.
33. Midander, K.; Cronholm, P.; Karlsson, H. L.; Elihn, K.; Möller, L.; Leygraf, C.; Wallinder, I. O. Surface Characteristics, Copper Release, and Toxicity of Nano- and Micrometer-Sized Copper and Copper(II) Oxide Particles: A Cross-Disciplinary Study. *Small* **2009**, *5*, 389–399.
34. Lastoskie, C.; Gubbins, K. E.; Quirke, N. Pore Size Heterogeneity and the Carbon Slit Pore: A Density Functional Theory Model. *Langmuir* **1993**, *9*, 2693–2702.
35. Samson, E.; Marchand, J.; Snyder, K. A. Calculation of Ionic Diffusion Coefficients on the Basis of Migration Test Results. *Mater. Struct.* **2003**, *36*, 156–165.
36. Jackler, R. K.; Parker, D. A. Radiographic Differential Diagnosis of Petrous Apex Lesions. *Am. J. Otol.* **1992**, *13*, 561–574.
37. Kircher, M. F.; Willmann, J. K. Molecular Body Imaging: MR imaging, CT, and US. Part I. Principles. *Radiology* **2012**, *263*, 633–643.
38. Sana, B.; Johnson, E.; Sheah, K.; Poh, C. L.; Lim, S. Iron-Based Ferritin Nanocore as a Contrast Agent. *Biointerphases* **2010**, *5*, FA48–FA52.
39. Sana, B.; Poh, C. L.; Lim, S. A Manganese-Ferritin Nanocomposite as an Ultrasensitive *T*₂ Contrast Agent. *Chem. Commun.* **2012**, *48*, 862–864.
40. Yan, G. P.; Robinson, L.; Hogg, P. Magnetic Resonance Imaging Contrast Agents: Overview and Perspectives. *Radiography* **2007**, *13*, e5–e19.
41. Tasis, D.; Tagmatarchis, N.; Bianco, A.; Prato, M. Chemistry of Carbon Nanotubes. *Chem. Rev.* **2006**, *106*, 1105–1136.

42. Lacerda, L.; Bianco, A.; Prato, M.; Kostarelos, K. Carbon Nanotubes as Nanomedicines: From Toxicology to Pharmacology. *Adv. Drug Delivery Rev.* **2006**, *58*, 1460–1470.

43. Robinson, J. T.; Tabakman, S. M.; Liang, Y.; Wang, H.; Casalongue, H. S.; Vinh, D.; Dai, H. Ultrasmall Reduced Graphene Oxide with High Near-Infrared Absorbance for Photothermal Therapy. *J. Am. Chem. Soc.* **2011**, *133*, 6825–6831.

44. Kam, N. W.; O'Connell, M.; Wisdom, J. A.; Dai, H. Carbon Nanotubes as Multifunctional Biological Transporters and Near-Infrared Agents for Selective Cancer Cell Destruction. *Proc. Natl. Acad. Sci. U.S.A.* **2005**, *102*, 11600–11605.

45. Wu, B.; Liu, Y.; Rose-Petrucci, C.; Diebold, G. J. X-ray Spatial Frequency Heterodyne Imaging. *Appl. Phys. Lett.* **2012**, *100*, 061110.

46. Woo, K.; Hong, J.; Choi, S.; Lee, H.; Ahn, J.; Kim, C. S.; Lee, S. W. Easy Synthesis and Magnetic Properties of Iron Oxide Nanoparticles. *Chem. Mater.* **2004**, *16*, 2814–2818.

47. Zhu, Y.; Jiang, F. Y.; Chen, K.; Kang, F.; Tang, Z. K. Size-Controlled Synthesis of Monodisperse Superparamagnetic Iron Oxide Nanoparticles. *J. Alloys Compd.* **2011**, *509*, 8549–8553.

48. Kim, F.; Luo, J.; Cruz-Silva, R.; Cote, L. J.; Sohn, K.; Huang, J. Self-Propagating Domino-like Reactions in Oxidized Graphite. *Adv. Funct. Mater.* **2010**, *20*, 2867–2873.

49. Guo, F.; Silverberg, G.; Bowers, S.; Kim, S.; Datta, D.; Shenoy, V.; Hurt, R. H. Graphene-Based Environmental Barriers. *Environ. Sci. Technol.* **2012**, *46*, 7717–7724.

50. Hayat, M. A. *Colloidal Gold: Principles, Methods and Applications*; Academic Press: San Diego, CA, 1989; Vols. 1 and 2.

51. Haynes, W. M. *CRC Handbook of Chemistry and Physics*; Taylor and Francis: Boca Raton, FL, 2012; pp 10–232.

52. Gomez-Navarro, C.; Weitz, R. T.; Bittner, A. M.; Scolari, M.; Mews, A.; Burghard, M.; Kern, K. Electronic Transport Properties of Individual Chemically Reduced Graphene Oxide Sheets. *Nano Lett.* **2007**, *7*, 3499–3503.